

Lead-Free α -La₂WO₆ Ferroelectric Thin Films

Thomas Carlier,[†] Marie-Hélène Chambrier,^{*,†} Anthony Ferri,[†] Sonia Estradé,[§] Jean-François Blach,[†] Gemma Martín,[§] Belkacem Meziane,[†] Francesca Peiró,[§] Pascal Roussel,[‡] Freddy Ponchel,^{||} Denis Rèmiens,^{||} Albert Cornet,[§] and Rachel Desfeux[†]

[†]Unité de Catalyse et de Chimie du Solide, UMR 8181 CNRS, Faculté des Sciences Jean Perrin, Université d'Artois, Rue Jean Souvraz, SP 18, F-62300 Lens, France

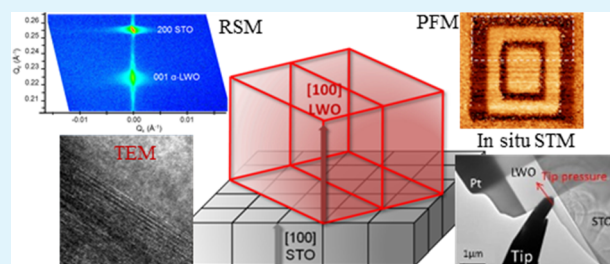
[‡]Unité de Catalyse et de Chimie du Solide, UMR 8181 CNRS, Ecole Nationale Supérieure Chimie Lille, Cité Scientifique, Bât C7, F-59652 Villeneuve d'Ascq, France

[§]LENS, MIND-In2UB, Electronics Department, Universitat de Barcelona (UB), Martí i Franquès 1, Barcelona 08028, Spain

^{||}Institut d'Electronique, de Microélectronique et de Nanotechnologies, DOAE, UMR 8520 CNRS, Université de Valenciennes et du Hainaut-Cambrésis, F-59313 Valenciennes 9, France

ABSTRACT: (001)-Epitaxial La₂WO₆ (LWO) thin films are grown by pulsed laser deposition on (001)-oriented SrTiO₃ (STO) substrates. The α -phase (high-temperature phase in bulk) is successfully stabilized with an orthorhombic structure ($a = 16.585(1)$ Å, $b = 5.717(2)$ Å, $c = 8.865(5)$ Å). X-ray-diffraction pole-figure measurements suggest that crystallographic relationships between the film and substrate are $[100]_{\text{LWO}} \parallel [110]_{\text{STO}}$, $[010]_{\text{LWO}} \parallel [1\bar{1}0]_{\text{STO}}$ and $[001]_{\text{LWO}} \parallel [001]_{\text{STO}}$. From optical properties, investigated by spectroscopic ellipsometry, we extract a refractive-index value around 2 (at 500 nm) along with the presence of two absorption bands situated, respectively at 3.07 and 6.32 eV. Ferroelectricity is evidenced as well on macroscale (standard polarization measurements) as on nanoscale, calling for experiments based on piezo-response force-microscopy, and confirmed with in situ scanning-and-tunneling measurements performed with a transmission electron microscope. This work highlights the ferroelectric behavior, at room temperature, in high-temperature LWO phase when stabilized in thin film and opens the way to new functional oxide thin films dedicated to advanced electronic devices.

KEYWORDS: pulsed laser deposition, high-resolution X-ray diffraction, transmission electron microscopy, ferroelectricity, piezoresponse force microscopy



INTRODUCTION

Piezoelectric and ferroelectric materials are of high interest in advanced electronic devices embodying an important part of industrial business. Their applications are widespread. These include sonars, frequency filters, gas ignitors, ultrasonic and medical diagnosis transducers, surveillance devices, and FeRAM memories, to name just a few amid so many other valuable usages.¹ Such a wide range of applications is rooted in the material electrical properties and stem from the nonsymmetrical organization of the atomic crystal configuration, usually referred to as the structure–properties relation.

In addition, environmental concerns call for the replacement of lead-based substances such as Pb(Zr,Ti)O₃ (PZT), (Pb,La)(Zr,Ti)O₃ (PLZT) or x Pb(MgNb)O₃-(1- x)PbTiO₃ (PMN-PT). However, it is well-known that these compounds are found in many electronic devices and are the most efficient at present. As a consequence, the current challenge involves investigations through new lead-free chemical systems based on the knowledge of the structure and tailoring properties at the atomic level.

On the other hand, lead-free oxides based on A₂O₃-MO₃ (A = Bi³⁺ or Ln³⁺; M = Mo or W) systems are of significant

technological interest owing to laser applications,² along with their ionic conduction,³ catalytic⁴ and ferroelectric properties.⁵ If we focus on the specific A₂MO₆ (A = Bi³⁺ or Ln³⁺; M = Mo or W) compounds, a wide range of bibliographical references related to studies on bulk materials exists. Also, the resulting crystal structure appears to depend on the exact method of synthetic preparation (sol-gel or solid-solid synthesis, heating treatments) yielding several polymorphic phases.^{6–10} These compounds typically present structural arrangements based on the fluorite (CaF₂) or Scheelite (CaWO₄) structure type.

Depending on the lanthanide (Ln) cation radius, three different tungstate structures are commonly observed for room temperature. Large radius cations (Ln = Ce to Dy) usually crystallize in a monoclinic fluorine superstructure (C^{2/c}; $a_M = 3a_F$; $b_M = 2b_F$; $c_M = c_F$ and $\beta = 107.7^\circ$); for smaller radius values (Ln = Ho to Lu) it results in the P^{2/c} space group.¹¹ Finally, the specific La₂WO₆ (LWO) compound is particular; bibliography is scarce and its two polymorphic structures, i.e., β -La₂WO₆

Received: February 27, 2015

Accepted: October 19, 2015

Published: October 19, 2015



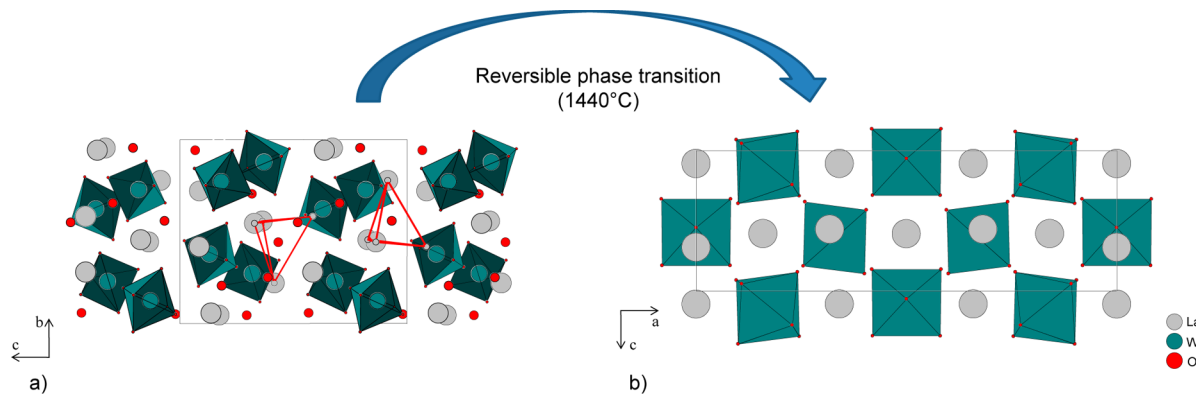


Figure 1. Structure projection of (a) low-temperature β - La_2WO_6 with $[\text{W}_2\text{O}_{11}]^{10-}$ blocs, two polyhedral $[\text{OLa}_4]^{10+}$ are evidenced (in red line); (b) high-temperature α - La_2WO_6 with isolated polyhedral $[\text{WO}_6]$.

(low temperature form) and α - La_2WO_6 (high temperature form) were solved only recently. The first reference concerning LWO was reported in the La_2O_3 – WO_3 phase diagram built by Rode et al.¹² in 1968, whereas the $\beta \rightarrow \alpha$ phase transition, at 1440 °C, was first mentioned by Yoshimura et al., in 1976.¹³

Thus, depending on temperature, this compound shows two structural arrangements (Figure 1). The low-temperature phase β - La_2WO_6 crystallizes in the space group $P2_12_12_1$ (No. 19) with cell parameters $a = 7.5196(1)$ Å, $b = 10.3476(1)$ Å, $c = 12.7944(2)$ Å.¹⁴ The structure consists of an octahedral $[\text{WO}_6]$ connected such that $[\text{W}_2\text{O}_{11}]^{10-}$ units are formed while the last oxygen atom is included in tetrahedral $[\text{OLa}_4]^{10+}$. β - La_2WO_6 structure is really original in comparison to all the other Ln_2MO_6 oxides. On the other hand, high-temperature form α - La_2WO_6 ,¹⁵ which crystallizes in the space group $Pm2_1n$ (No. 31) with cell parameters $a = 16.5531(1)$ Å, $b = 5.52003(3)$ Å, $c = 8.88326(3)$ Å, presents a close relation with Scheelite and $\text{Lu}_{0.8}\text{Nd}_{1.2}\text{WO}_6$ structures.¹⁶ Its orthorhombic structure is described with two kinds of octahedral $[\text{WO}_6]$ in which the entity $[\text{OLa}_4]$ has disappeared in comparison to the β - La_2WO_6 structure. From an electrical point of view, electrical-impedance spectroscopy measurements were carried out on these two polymorphs. Both showed insulator-like behaviors and characteristics.^{14,15}

To the best of our knowledge, no work has ever been focused on both the synthesis of LWO as a thin film and the investigation of piezo-/ferroelectric properties, despite the fact that the two polymorphs of this compound may present potential interests owing to the above specified functional properties. Indeed, owing to the fact that they crystallize in $Pm2_1n$ (α - La_2WO_6) and $P2_12_12_1$ (β - La_2WO_6) space groups, which correspond to noncentrosymmetric $m\bar{m}$ and 222 class crystalline-structures, respectively, these yield potential interesting properties such as ferroelectricity (for a review, see K.R. Poeppelmeier et al.).¹⁷ Moreover, since the 1980s, ferroelectric thin films have attracted an increasing interest due to the crossing of two phenomena: their integration into micro-electronic devices such as nonvolatile memories and integrated optics with the help of high-quality thin-film growth-techniques. Among these, pulsed laser deposition (PLD) appears to be one of the most efficient and easiest routes that lead to the growth of high-quality thin films with numerous potential applications, ranging from integrated circuits and optoelectronics to micromechanics.¹⁸ Moreover, structural film-deposition parameters during PLD experiments may be easily

modified and controlled, thus leading to the stabilization of initially metastable phases.^{19–23}

This paper aims at reporting the growth of LWO thin films using the well-known PLD technique. The films were characterized through X-ray diffraction (XRD) and Transmission Electron Microscopy (TEM). Spectroscopic ellipsometry measurements were carried-out in order to extract optical indexes and film thicknesses, while determining both the absorption band and the direct band gap. Piezoelectric and ferroelectric properties were investigated on the nanometer scale by means of piezoelectric force microscopy (PFM) along with a TEM equipped with a scanning tunneling microscope (STM) in situ holder.

EXPERIMENTAL SECTION

A 10 g pellet was synthesized starting with the oxides La_2O_3 and WO_3 , weighted in stoichiometric proportions and ground together in an agate mortar. Before crushing, the lanthanum oxide powder was first dried and decarbonated at 1000 °C, overnight. The prepared composition was then heated at 1350 °C, during one complete night, in an alumina crucible, before cooling it down. This procedure was repeated twice to ensure more reliable results. The ground powder was compelled into pellets (1 in. diameter) with the help of uniaxial pressure and finally annealed at 1450 °C for 12 h in air before letting it slowly cool down toward room temperature. At each grinding step, X-ray diffractograms were recorded in order to check out the powder purity. Finally, the obtained β - La_2WO_6 pellet was used as a target in the film deposition step.

In order to optimize synthesis parameters, LWO thin films were first deposited on (100)-oriented SrTiO_3 (STO) single-crystal substrates (Crystal GmbH, Germany) and then grown on semiconducting (100)-oriented Nb-doped (1.4 at %) STO single-crystal substrates (Crystal GmbH, Germany) to allow for electrical measurements. All substrates were first ultrasonically cleaned in ethanol for 5 min, and then dried. The pressure in the pulsed-laser chamber was lowered down to 1×10^{-6} mbar and the substrate temperature for the film growth raised through a 10 °C/min step elevation toward synthesis temperature (three temperatures were tested: 600, 800, and 900 °C) while adjusting the O_2 pressure during deposition to 1×10^{-3} mbar or 1×10^{-1} mbar. Finally, at the end of deposition, the O_2 pressure was increased up to 200 mbar in the chamber and next, the films were slowly cooled to room temperature.

Depositions were carried out with a Compex Pro 102 KrF excimer laser ($\lambda = 248$ nm). All films (single layers on bare substrates) were grown using 5000 laser-pulse shots. The fluence was adjusted to 2 J/cm² and the deposition rate fixed at 2 Hz. The target-substrate distance was adjusted to $d = 4.5$ cm.

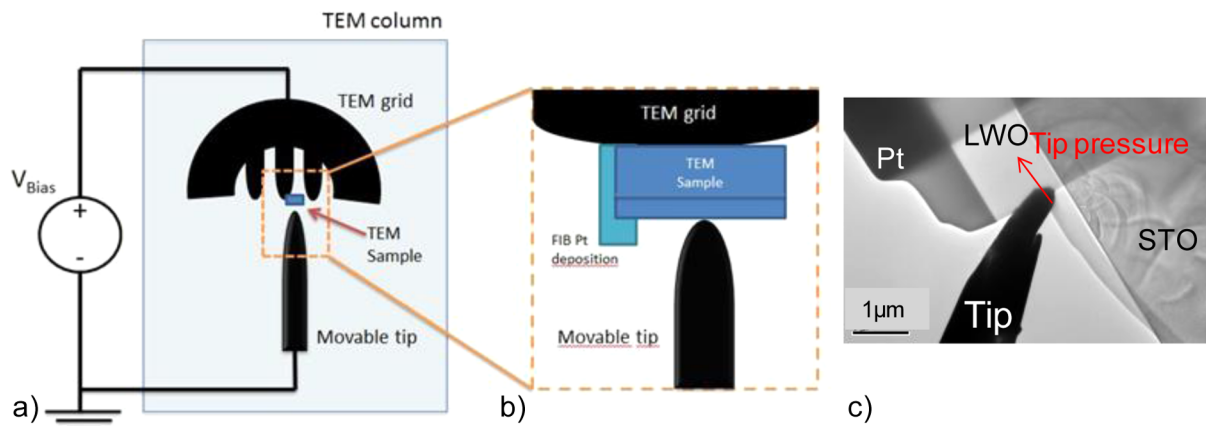


Figure 2. (a) Schematic representation and (b) zoomed portion on the tip of in situ TEM-STM system; (c) TEM image of the platinum tip, contacting the sample.

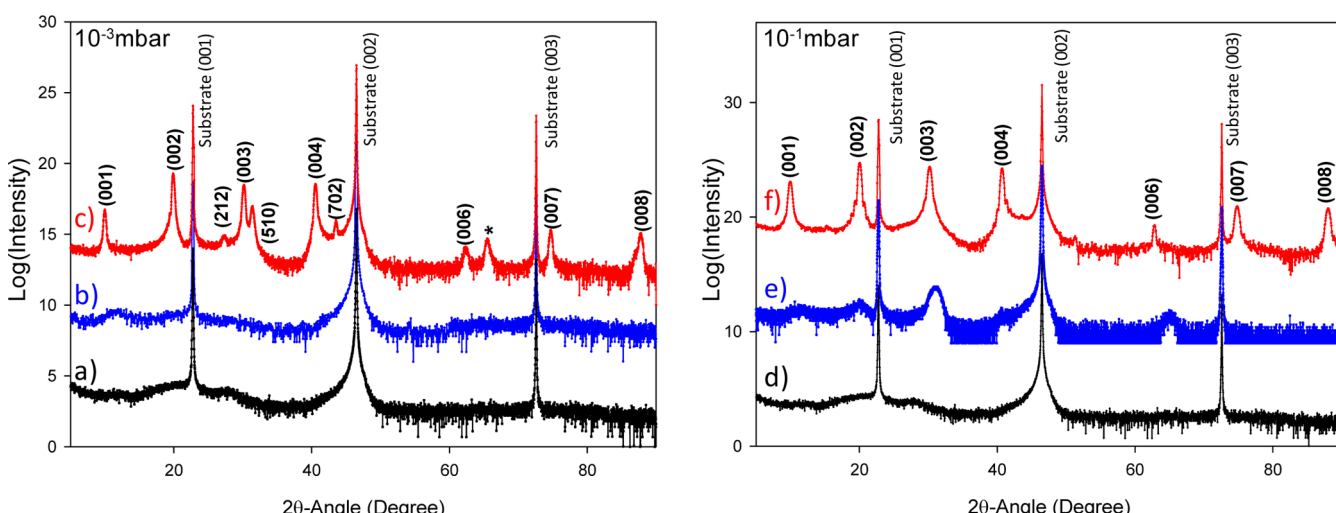


Figure 3. X-ray diffractograms showing the effect of temperature T and pressure P in obtaining epitaxial $\alpha\text{-La}_2\text{WO}_6$ thin film. (a) $T = 600$ °C and $\text{PO}_2 = 1 \times 10^{-3}$ mbar; (b) $T = 800$ °C and $\text{PO}_2 = 1 \times 10^{-3}$ mbar; (c) $T = 900$ °C and $\text{PO}_2 = 1 \times 10^{-3}$ mbar (the star corresponds to an unidentified peak); (d) $T = 600$ °C and $\text{PO}_2 = 1 \times 10^{-1}$ mbar; (e) $T = 800$ °C and $\text{PO}_2 = 1 \times 10^{-1}$ mbar; (f) $T = 900$ °C and $\text{PO}_2 = 1 \times 10^{-1}$ mbar.

The powder X-ray diffractograms were obtained with a Rigaku Ultima IV equipped with a Cu-anode X-ray ($\lambda_{\text{K}\alpha 1} = 1.54056$ Å, $\lambda_{\text{K}\alpha 2} = 1.54443$ Å).

The thin film crystalline nature (indexation, crystalline quality and pole figures) was characterized using a Rigaku SmartLab high resolution X-ray diffractometer equipped with a 9 kW rotating anode X-ray generator ($\lambda_{\text{K}\alpha 1} = 1.54059$ Å). The X-ray beam was made parallel with cross-beam optics and monochromatized with a double Ge (220) monochromator. In this study all the ($2\theta - \omega$) scans were performed in the range 10–80°, with a step size of 0.02° and a 1°/min speed.

TEM experiments were carried out using a JEOL 2010F (200 kV), with a lateral resolution of 0.19 Å, equipped with a STM holder for in situ electrical probing.²⁴ A sharp platinum tip was attached to the movable part of the STM holder and piezo-electrically controlled. Both the sample and the tip were oriented perpendicular to the electron beam of the TEM (Figure 2). The probe may be positioned in a millimeter-scale workspace with subnanometer resolution, thus enabling the selection of a specific nanostructure and the application of some voltage to perform electrical measurements. TEM samples were prepared by Focused Ion Beam using the lift-out technique.

The macroscopic ferroelectric loops $P(E)$ were measured at room temperature on $\text{LaNiO}_3/\text{LWO}/\text{Pt}$ capacitors, using a standardized Radiant RT6000 system. The LWO film (300 nm-thick about) was grown by pulsed laser ablation on a 200 nm-thick metallic (001)-oriented LaNiO_3 bottom electrode previously deposited on bare

substrate by rf magnetron sputtering. The sputtering conditions for LNO deposition may be found elsewhere.²⁵ Dots of Pt electrodes, 150 μm in diameter, were sputtered on the top surface of the LWO films through a metallic shadow mask (lift-off process). For measurement of hysteresis loop, the charge option was used; the Pt top electrode was always connected to the drive terminal of the test equipment, whereas the LNO bottom electrode was connected to the return terminal. The frequency measurement was fixed to 10 kHz and a DC electric field was applied to the film.

The surface morphology and nanoscale piezo-/ferroelectric properties of the films were investigated using commercial atomic force microscope (AFM) (MFP-3D, Asylum Research) working in contact mode under environmental conditions. Switching behavior for ferroelectric domains was probed by locally manipulating domains while piezoelectric-activity was measured by recording characteristic hysteresis loops. Statistical study for piezoloops measurements was carried out, i.e., 50 loops were measured over the film surface and the loops shown in this work are representative of the average response of the active layer. All of the remnant piezoresponse loops were recorded over a period of 5 s, with duration for pulses and zero field of 50 ms. Ti/Ir conductive tips coating (Asylum Research ASY-ELC-01 probes, $k \approx 2 \text{ N m}^{-1}$) and ground conductive substrates were used to perform these experiments. Detailed information pertaining to further PFM working conditions may be found elsewhere.^{26,27}

Spectroscopic ellipsometry (SE) measurements were performed at room temperature using a phase-modulated ellipsometer (UVISEL

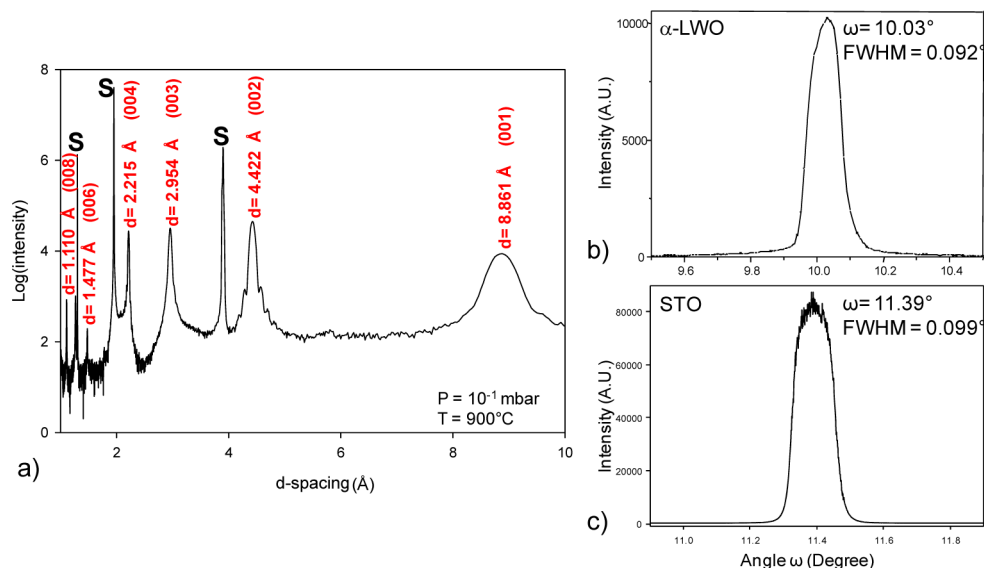


Figure 4. (a) d -spacing, X-ray diffractogram and (00l) $\alpha\text{-La}_2\text{WO}_6$ indexation. Pendolensung fringes are visible on (002) peak. (b) Rocking curve on (002) $\alpha\text{-LWO}$ -thin film. (C) Rocking curve on (001) STO substrate.

HR460 from Horiba Scientific) at wavelengths ranging from 260 to 1500 nm with 2 nm spectral interval. An incidence angle of 70° was used for all measurements. The raw signal measured by SE has the following form

$$I(t) = I_0 + I_S \sin(\delta(t)) + I_C \cos(\delta(t)) \quad (1)$$

Where $\delta(t)$ is a phase shift. In our experimental configuration, the value of I_0 , I_C , and I_S are linked to the ellipsometric angles (Δ , Ψ) by the following relations

$$I_0 = 1 \quad (2)$$

$$I_S = \sin 2\Psi \sin \Delta \quad (3)$$

$$I_C = \sin 2\Psi \cos \Delta \quad (4)$$

The ellipsometric angles Δ and Ψ are related to the complex reflection coefficients of polarized light: R_p and R_s for a polarization parallel and perpendicular to the plane of incidence, respectively. For each sample, the measured spectra may be analyzed using an appropriate fitting model based on sample structure. All fitting steps were performed using the Delta-Psi Horiba software.²⁸

RESULTS AND DISCUSSION

X Ray Diffraction Phase. Because there were no previous studies about pulsed laser deposition of LWO, the first step consisted in optimizing the thin film growth conditions. For such a purpose, both the temperature of the substrate and the O₂ pressure during deposition were optimized in order to increase the thin-film quality.

XRD diffractograms were acquired at three different deposition temperatures, ranging from 600 to 900 °C on (100)-oriented STO substrates (Figure 3). For the lowest temperature considered, i.e., 600 °C, no crystalline peak is observed, implying an amorphous film. Increasing the pressure from 10⁻³ to 10⁻¹ mbar has no influence on crystallization (Figure 3a, d). At 800 °C, the O₂ pressure plays an important role: whereas the thin film is still amorphous under a pressure of 1 × 10⁻³ mbar, some XRD peaks with large full width at half maximum (FWHM) appear under a pressure of 1 × 10⁻¹ mbar (Figure 3b, e). Finally, at 900 °C for the two tested pressures, 1 × 10⁻³ and 1 × 10⁻¹ mbar, well-defined families of XRD peaks emerge (Figure 3c, f). Such an observation at this rather high

temperature is not surprising when taking into account the refractive behavior of these oxides. However, the number of diffraction peaks that are observed on the diffractograms appears rather limited, compared to the ones obtained in the case of bulk materials. As a result, the indexation may only carry some signature conferring the $\alpha\text{-La}_2\text{WO}_6$ composition to the obtained thin films.

Considering the film grown at 900 °C under an O₂ pressure of 10⁻¹ mbar (Figure 3f), we show the possibility to grow highly oriented *c*-axis $\alpha\text{-LWO}$ thin films. This XRD pattern leads us toward the stage of phase identification. Indeed, Figure 4 shows that the diffractogram (900 °C; 1 × 10⁻¹ mbar), represented as a function of d -spacing, points out toward a harmonic-peak series, which corresponds to (00l) planes of $\alpha\text{-La}_2\text{WO}_6$, in accordance with the ICDD-PDF card found by using the identification software EVA (Bruker). Similar results are obtained for thin film grown on (100)-oriented Nb-doped (1.4 at %) STO substrate. These results demonstrate that the high-temperature $\alpha\text{-LWO}$ polymorph may be stabilized at room temperature in thin film by PLD, by considering the $\beta\text{-LWO}$ phase as the starting material for the target. In fact, such stabilization may be attributed to the good compatibility between the film/substrate crystal lattices. With the *a* and *b* lattice parameters of the $\alpha\text{-LWO}$ compound (values that have been obtained from a previous powder study¹⁵), we have calculated the lattice mismatch δ and δ' as follows

$$\delta = \frac{3a_{\text{STO}}\sqrt{2} - a_{\text{LWO}}}{3a_{\text{STO}}\sqrt{2}} \times 100 \quad (5)$$

$$\delta' = \frac{a_{\text{STO}}\sqrt{2} - b_{\text{LWO}}}{a_{\text{STO}} \times \sqrt{2}} \times 100 \quad (6)$$

with $a_{\text{STO}} = 3.905$ Å in the case of STO commercial substrate (Crystal GmbH); $a_{\text{LWO}} = 16.5513$ Å and $b_{\text{LWO}} = 5.5200$ Å.

As a result, we find $\delta = 9.78 \times 10^{-2}$ % and $\delta' = 4.53 \times 10^{-2}$ %. The values of the lattice mismatch δ and δ' are really weak in the case of (001)-oriented STO substrates. These low lattice mismatches indicate a possible matching of a_{LWO} and b_{LWO} on STO.

Epitaxy Relationships. To get a better insight on the microstructural properties of α -LWO, we determined an evaluation of the mosaicity of the thin film, with respect to the normal to the substrate, by performing an X-ray rocking curve for the (001) reflection (Figure 4b). Indeed, from a $2\Theta_{\text{Bragg}}$ angle and a slight variation of ω , all coherent domains around the $2\Theta_{\text{Bragg}}$ position would result in a diffraction phenomenon, thus an intensity distribution should be observed, as expected from the relative disorientation of coherent domains normal to the substrate. On (100)-STO, the FWHM is around 0.092° , which indicates a high crystalline quality with a weak disorientation of the coherent domain, of the same order of magnitude as the FWHM obtained from (100)-STO (Figure 4c). This mosaicity highlights a rather good quality of the film, with not much out-of-plane (OP) disorientation, probably due to a good lattice match between α -LWO and STO.

To check for the possible presence of domains, we have also undertaken a φ scan of the (111) reflection on α -LWO (Figure 5). This plane diffracts at $2\Theta_{\text{Bragg}} = 19.66^\circ$ and the χ angle

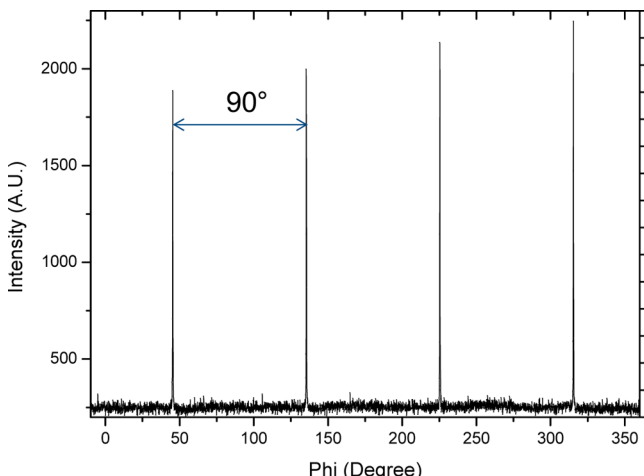


Figure 5. Phi-scan for α - La_2WO_6 on (111) peak. Peak repetition rate is 90° , showing an orthorhombic symmetry.

between (001) and (111) is 59.247° (calculated from Carine software²⁹). Four peaks are observed with a 90° angular-gap between two consecutive ones, as expected from a single-domain film-growing with an orthorhombic symmetry.

A pole figure was performed in order to convey the epitaxial relationships and provide the complete orientation of the film with respect to the substrate. We have chosen the (315) reflection of α -LWO ($2\Theta = 57.79^\circ$) for two main reasons: (i) it is close to (112) substrate reflection, enabling a relative orientation in only one measurement, (ii) because of its relatively higher intensity. Results are shown on the stereogram seen in of Figure 6a. From straightforward comparison between simulated results obtained with the software Stereopole, and the observed pole figure, one may deduce that our film presents a 3-D heteroepitaxy with the following epitaxial relationships: $[100]_{\text{LWO}} \parallel [110]_{\text{STO}}$, $[010]_{\text{LWO}} \parallel [1\bar{1}0]_{\text{STO}}$, and $[001]_{\text{LWO}} \parallel [001]_{\text{STO}}$ (Figure 6c).

A reciprocal space map (RSM) was also acquired and shows that the α -LWO thin film is fully clamped on the substrate; indeed a perfect vertical alignment between the thin film and substrate reflections is observed (Figure 6b). We also located the exact position of the (305) ($2\Theta = 54.29^\circ$) and (017) ($2\Theta =$

77.07°) reflections in order to extract the thin film cell parameters of α -LWO. Combining with the value obtained for c from $2\theta-\omega$ X-ray diffractogram ($c = 8.865(5)$ Å), we deduced the a and b thin film parameters, whose values reach $16.585(1)$ and $5.717(2)$ Å, respectively.

Epitaxial relationships were also confirmed by high-resolution TEM images (Figure 7). A good thin-film crystallinity was evidenced with no amorphous areas at the interface between the film and substrate. On the other hand, a α -LWO film thickness for film close to 40 nm was determined.

Thickness Measurements. From an optical point of view, LWO film deposited on STO substrate can be considered as a two-layer model (Figure 8a): a semi-infinite STO substrate and a dense layer of α -LWO. In order to obtain a reliable model, the first step consists in finding the optical functions of each layer (Figure 8a). The optical function of STO was obtained calling for measurements performed on a STO single crystal substrate. After recording experimental data, we use a point-by-point calculated model to directly extract the value of n and k (i.e., the real and imaginary part of the optical index, respectively). On the other hand, optical function of α -LWO layer was determined by fitting the ellipsometric spectra obtained with a sample layer deposited on STO substrate. The optical function of α -LWO was chosen as the sum of double Lorentz isotropic oscillators of the following form

$$\epsilon = \epsilon_\infty + \frac{(\epsilon_s - \epsilon_\infty)\omega_t^2}{\omega_t^2 - \omega^2 + i\Gamma_0\omega} + \frac{f_1\omega_0^2}{\omega_0^2 - \omega^2 + i\gamma_1\omega} \quad (7)$$

It is worth pointing out that our ellipsometric spectra measurements were not sensitive to the rotation of the sample: therefore, anisotropic effects have been neglected in our model. To the best of our knowledge, this is the first time that the optical properties of this material have been determined. After some fitting process, we found that the optical function, in the 260–1500 nm range, is the sum of two oscillators with absorption bands lying, respectively, at 3.07 and 6.32 eV. The evolution in the visible-NIR range of the dielectric function ($\epsilon = \epsilon_r + i\epsilon_i$) of the thin film deposited onto STO substrate is presented Figure 8b. The parameters of the optical function are given in Table 1. The thickness was determined with the same fitting procedure and we found an approximate value of 37 nm. This value is in good agreement with the one measured by TEM.

Macroscale Ferroelectric Properties. Figure 9 shows characteristic $P(V)$ hysteresis loops measured at room temperature on (100)LNO/(100) α -LWO/Pt capacitors. As a result, we notice a limit in the DC voltage, since from 15 V (corresponding to an applied electric field of about 500 kV·cm⁻¹), we systematically observe the breakdown of the film. For the maximum applied electric field, the remnant polarization remains very weak (P_s is about $3 \mu\text{C}\cdot\text{cm}^{-2}$ under 500 kV·cm⁻¹). The main reason could be the domains pinning effect preventing the switch of the polarization. This behavior is confirmed by the nanoscale study described below. Further investigations are required to better understand this polarization degradation.

Nanoscale Ferroelectric Properties. A characteristic image of the film surface morphology, as recorded by AFM, is shown in Figure 10a. As observed, the surface is represented by rounded grains whose diameter value lies somewhere between 100 and 200 nm. The root mean-square roughness for a $10 \times 10 \mu\text{m}^2$ scan area was measured to be around 2.2 nm.

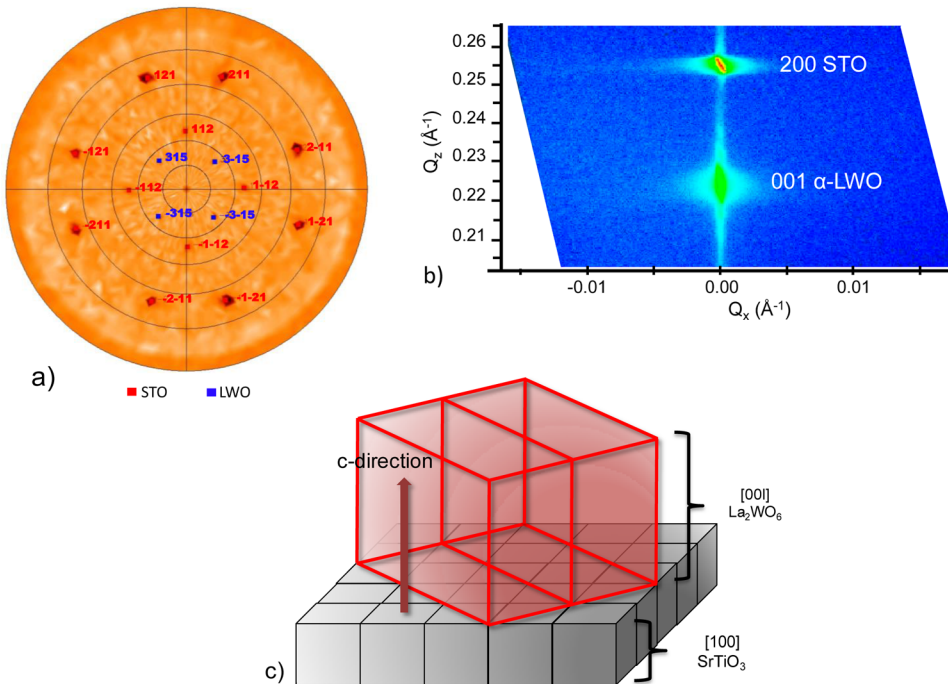


Figure 6. (a) α -La₂WO₆ (315) Pole figure, illustrating the orientation relationship between STO-(100) substrate and α -La₂WO₆ thin film; (b) reciprocal space map, along 200 STO and 001 α -LWO; (c) epitaxy relationships scheme.

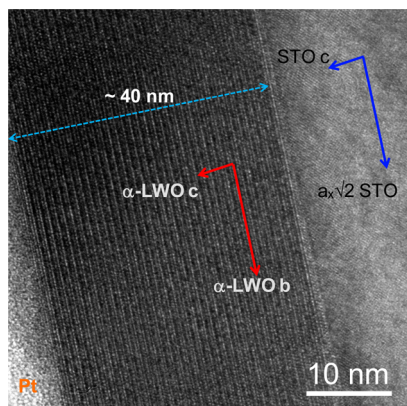


Figure 7. High-resolution transmission-electron-microscopy image of the interface. The α -LWO thin film thickness is shown.

Table 1. Parameters of Optical Function of α -La₂WO₆

ε_{∞}^a	ε_s^a	ω_t^c (eV)	Γ_0 (eV) ^d	f_1^b	ω_{01}^c [eV]	γ_1^d [eV]
1	3.37	6.32	1.27	0.23	3.07	1.97

^a ε_{∞} , ε_s are, respectively, the high-frequency dielectric-constant and the value of the dielectric function, at zero frequency. ^b f_1 corresponds to the strength of the second Lorentz oscillator. ^c ω_t and ω_{01} are the resonant frequencies of the oscillators, whose energies correspond to absorption peaks. ^d Γ_0 and γ_1 are the broadening (damping factor) of each oscillator.

Local ferroelectric properties were investigated by PFM. Figures 10b, c display the OP-phase and OP-amplitude images, simultaneously recorded by using dual AC resonance tracking (DART) PFM.³⁰ Four “artificial” rectangular-shaped domains of downward (black contrasts, 5.5×5 and $3 \times 2.5 \mu\text{m}^2$) and upward (white contrasts, 4.5×3.5 and $2.2 \times 1.5 \mu\text{m}^2$) polarization were locally and alternatively written by applying a DC voltage of +10 V and -10 V to the AFM tip, respectively.

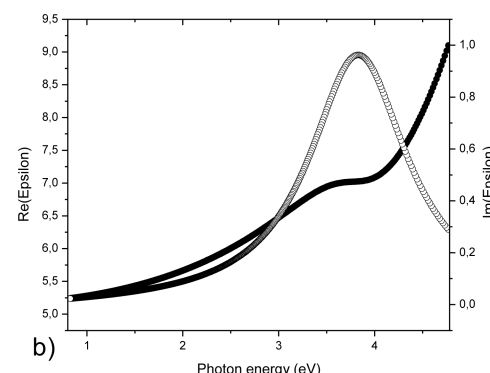
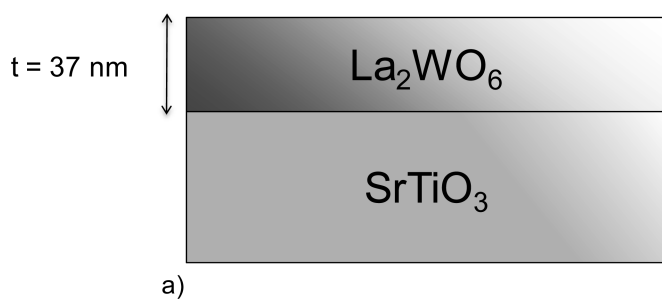


Figure 8. (a) Model of La₂WO₆ thin film, used in spectroscopic ellipsometry for optical measurements; (b) real part (solid circle) and imaginary part (open circle) of dielectric function ε as a function of photon energy.

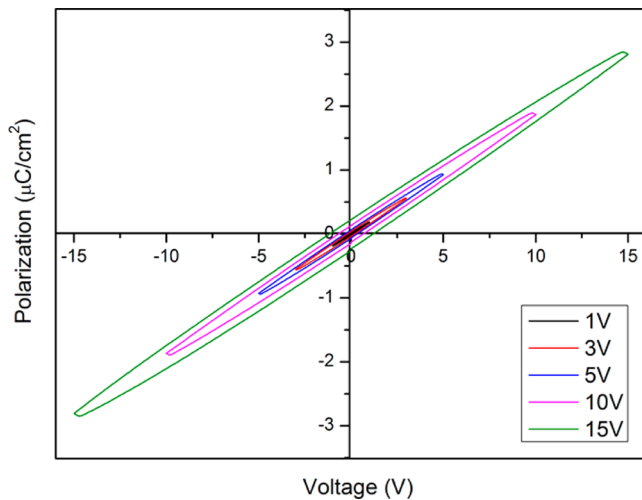


Figure 9. $P(V)$ hysteresis loops of LNO/LWO (300 nm)/Pt capacitors measured at $f = 10$ kHz and under an applied voltage of 1, 3, 5, 10, and 15 V.

Polarization switching is successfully performed, as evidenced by both the well-defined rectangles and the high contrasts obtained after poling experiments. Below the phase image is depicted the signal distribution for area delimited by the dashed rectangle corresponding to the two oppositely poled regions (Figure 10d). A phase difference of almost 180° is obtained suggesting fully switching of domains to one of the two c -oriented polarization states. In addition, these polarized domains have been imaged several hours after the switching experiment, thus demonstrating that the signal measured by PFM is mainly due to the ferroelectric polarization, and not by possible injected charges coming from the probe tip. The Figure 10c reveals high contrasts corresponding to the vibration amplitude of the manipulated domains. Clear domain boundaries are evidenced with areas revealing no amplitude signal, due to the change of polarization. The similar magnitude of the piezosignal observed for two polarized domains suggests relatively homogeneous electromechanical properties of the film.

To further address the local switching behavior of ferroelectric domains, as well as the piezo-activity, we measured piezo-response loops by placing the AFM tip over the free film surface. Off-field phase and amplitude loops are depicted in Figures 11a, b, respectively. In this procedure, each point was measured at zero bias voltage to promote the electromechanical contribution at the expense of the electrostatic effect, which corresponds to the remnant response.^{31–33} Square hysteresis response is clearly obtained from the phase signal (Figure 11a). Both the two opposite polarization states and the hysteretic behavior strongly reveal the local ferroelectricity in the as-deposited $\alpha\text{-La}_2\text{WO}_6$ thin film. We can also note the high coercive voltage (about 6.5 V) if we consider the relatively low thickness of the layer (~ 40 nm). Indeed, although remnant measurements lead to higher coercive voltage compared to the in-field mode, our value can evidence the difficulty to switch the domains, which is in agreement with the obtained $P(V)$ hysteresis loop. Besides, a well-defined typical butterfly shape due to the inverse piezoelectric effect is observed for the simultaneously recorded amplitude piezo-loop (Figure 11b), evidencing the local piezo-activity of the film. In addition, a saturated loop is measured without a linear part, an indication of the strong electromechanical contribution to the detected piezo-signal. As a remark, we note a shift toward positive voltage-values, along the horizontal axis, for both phase and amplitude loops, which points toward an imprint phenomenon of the local switching, attributed to an internal built-in electric field that already exists inside the film.^{34,35} A slight asymmetry in the tip vibration-amplitude along the vertical axis is also observed. This may be explained by the difference between the work functions of the probing tip and the conductive substrate, resulting in an internal bias field.³⁶ This asymmetry was previously observed on PZT and $\text{La}_2\text{Zr}_2\text{O}_7$ thin films.^{37,38} As a consequence, both the remnant upward- and downward-poled domains and the clear hysteretic dependence of the remnant phase and amplitude signals highlight the intrinsic local piezo-/ferroelectric nature of the $\alpha\text{-La}_2\text{WO}_6$ film.

Finally, the piezo-/ferroelectricity was further investigated at the local scale by means of *in situ* TEM-STM electrical experiments. The first step of the experiment was to characterize the conductivity through the FIB platinum

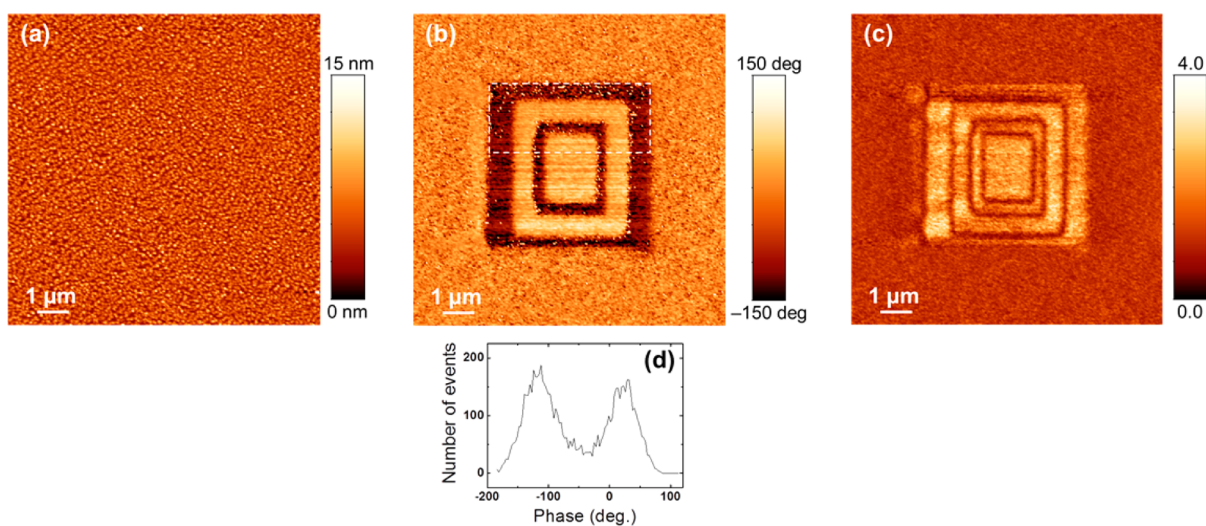


Figure 10. (a) AFM topographic image, (b) OP-phase image, and (c) OP-amplitude image, simultaneously recorded on the $\alpha\text{-La}_2\text{WO}_6$ film. (d) Histogram of the phase signal for area in dashed rectangle on the phase image.

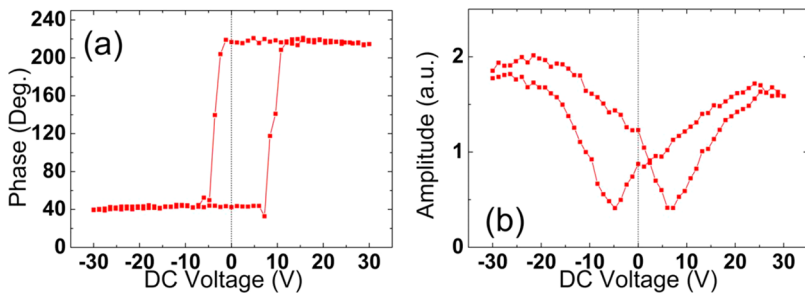


Figure 11. Remnant (a) phase and (b) amplitude hysteresis loops, simultaneously measured on the free surface of the $\alpha\text{-La}_2\text{WO}_6$ thin film.

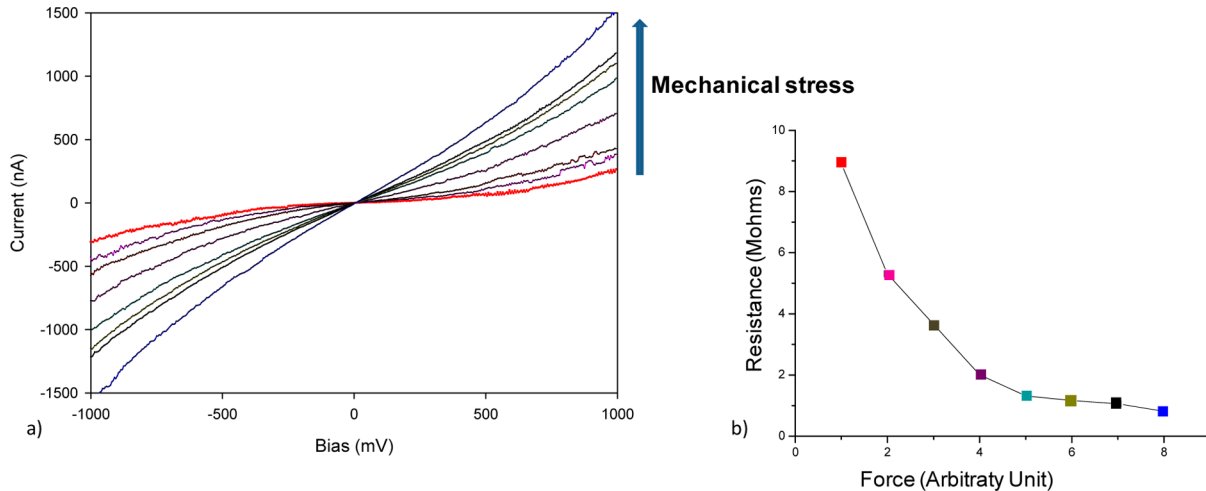


Figure 12. (a) Characteristic local $I\text{-}V$ curves for increasing pressures applied with STM tip to sample surface, and (b) electrical resistance calculated in the linear region vs force applied with STM tip to sample surface for $\alpha\text{-La}_2\text{WO}_6$. As it is not possible to know the exact value of the force applied with the tip with this experimental setup, each mechanical step of the tip position is used as a measurement unit.

deposition (see Figure 2) in order to ensure good sample preparation that prevents any short-circuit. The resistance through the FIB platinum deposition is about $500\ \Omega$, which shows that the system allows for good electrical conduction through the sample.

Further qualitative characterization of the piezoelectric behavior was carried out by measuring the $I\text{-}V$ curves while pressure was applied by the STM tip to the sample. Unlike the PFM experiments, where electric voltage is applied to the layer, this *in situ* TEM measurement enables us to probe the direct effect of the piezoelectricity, i.e., the generated electrical energy (or current) following the application of some mechanical stress. As it is not possible to accurately quantify the force applied with the employed TEM-STM system, we used, as a measurement unit, each mechanical step of the tip position. For each position, as controlled with the holder piezoelectricity, we recorded a characteristic local $I\text{-}V$ curve. The local conductivity-variations through the $\alpha\text{-LWO}$ film, as a function of mechanical stress, were measured, and the results are shown in Figure 12. The $I\text{-}V$ red curve corresponds to the minimum force which may be applied to allow electrical contact. We observe a clear increase of the conductivity when higher pressure is applied to the LWO surface. In addition, the resistance values were calculated from the ohmic region of each $I\text{-}V$ characteristics, and plotted on the inset of Figure 12. A decrease in the resistance, from $9\ \text{M}\Omega$ (red curve) to $800\ \text{k}\Omega$ (blue curve) is observed as more pressure is applied by the nanometric tip to the sample. Although there have recently been publications regarding mechanical pressure induced

changes in signals and bias induced ionic motion,^{39,40} this effect can be considered negligible for this type of electrical resistance measurements. These specific evolutions in local conductivity and resistance, with respect to the mechanical stress induced by the tip, are the signature of the direct effect of the piezoelectricity that occurs in the LWO thin film.

Figure 13 shows the half-cycle of the hysteresis switching current, obtained with the $I\text{-}V$ measurement method by

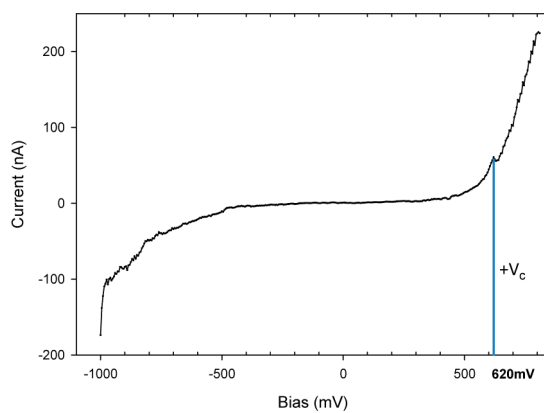


Figure 13. Half-cycle of the hysteresis switching current obtained with the $I\text{-}V$ measurement method by applying the minimum pressure allowing electrical contact for $\alpha\text{-La}_2\text{WO}_6$. A jump of current is observed for a voltage bias of $620\ \text{mV}$, a value that corresponds to coercive voltage.

applying the minimum pressure that allows electrical contact. As a result, we observe a jump of the current value, for a 620 mV bias voltage. In fact, this jump exists for a ferroelectric film, when the applied voltage is close to the coercive level.⁴¹ This current peak corresponds to the dipole-reorientation contribution of the ferroelectric material, which shows a state of ferroelectricity inside the α -LWO layer.

CONCLUSION

In this study, we have demonstrated that a high-temperature phase in a bulk material, namely the α -La₂WO₆ phase, can be successfully stabilized in thin films, on (001)-oriented SrTiO₃ substrate by pulsed laser deposition. Pole figures and reciprocal space maps give evidence of an epitaxial film-growth on the substrate. Rocking-curves measurements confirm the high quality of the film, whereas high-resolution electron-microscopy images reveal a perfect interface between the film and the substrate. These results are explained by taking into account the good film–substrate lattice match. On the other hand, the direct and converse effects of piezoelectricity, as well as ferroelectric properties on macro and nanoscale, are highlighted, at room temperature, in this oxide by both piezo-response PFM experiments and TEM studies, coupled with an *in situ* STM analysis. To conclude, this new lead-free α -LWO advanced phase, stabilized in thin film, may be considered as a promising candidate for nanodevice applications.

AUTHOR INFORMATION

Corresponding Author

*E-mail: mh_chambrier@yahoo.fr.

Author Contributions

The manuscript was written through contributions of all authors. All authors have given approval to the final version of the manuscript.

Notes

The authors declare no competing financial interest.

ACKNOWLEDGMENTS

The authors would like to acknowledge L. Burylo and F. Capet for their technical support on XRD and A. Verbeke for her help. A. Da Costa is acknowledged for technical support and discussions about AFM experiments. D. Troadec is gratefully acknowledged for F.I.B experiments. The “Fonds Européen de Développement Régional (FEDER)”, “CNRS”, “Région Nord-Pas de Calais” and “Ministère de l’Education Nationale de l’Enseignement Supérieur et de la Recherche” are acknowledged for fundings of X-ray diffractometers. The “Région Nord-Pas de Calais” and the “Fonds Européen de Développement Régional (FEDER)” under the “Contrat de Plan État-Région (CPER)” project “Chemistry and Materials for a Sustainable Growth” is gratefully acknowledged for funding of MFP-3D microscope. T. Carlier is grateful to the Nord-Pas de Calais region for its financial support to carry out this work. The Scientific and Technological Centers of Universitat de Barcelona are acknowledged. The authors also thank the financial support by the Spanish Government (IMAGINE-Consolider 2009CSD-00013 and MAT2010-16407 projects).

REFERENCES

- (1) Haertling, G. H. Ferroelectric Ceramics: History and Technology. *J. Am. Ceram. Soc.* **1999**, *82*, 797–818.
- (2) Senthil Kumaran, A.; Babu, S. M.; Ganeshamoorthy, S.; Bhaumik, I.; Karnal, A. K. Crystal Growth and Characterization of KY(WO₄)₂ and KGd(WO₄)₂ for Laser Applications. *J. Cryst. Growth* **2006**, *292*, 368–372.
- (3) Lacorre, P.; Goutenoire, F.; Bohnke, O.; Retoux, R.; Laligant, Y. Designing Fast Oxide-Ion Conductors Based on La₂Mo₂O₉. *Nature* **2000**, *404*, 856–858.
- (4) Knight, K. S. The Crystal Structure of Russellite; a Re-Determination Using Neutron Powder Diffraction of Synthetic Bi₂WO₆. *Mineral. Mag.* **1992**, *56*, 399–409.
- (5) Borchardt, H. J.; Bierstedt, P. E. Ferroelectric Rare Earth Molybdates. *J. Appl. Phys.* **1967**, *38*, 2057–2060.
- (6) Efremov, V. A.; Tyulin, A. V. Polymorphism of Oxytungstates Tr₂WO₆. Mechanism of Structural Changes of Er₂WO₆. *Kristallografiya* **1987**, *32*, 363–370.
- (7) Efremov, V. A.; Tyulin, A. V. Polymorphism of Oxytungstates Tr₂WO₆. Analysis of Structural Type II (Gd₂WO₆ and Gd₂MoO₆). Mechanism of Structural Change in Gd₂WO₆ in the Phase Transition II \leftarrow V. *Kristallografiya* **1987**, *32*, 371–377.
- (8) Polyanskaya, T. M.; Borisov, S. V.; Belov, N. V. A New Form of the Scheelite Structural Type: Crystal Structure of Nd₂WO₆. *Dokl. Akad. Nauk SSSR* **1970**, *193*, 83–86.
- (9) Tyulin, A. V.; Efremov, V. A.; Trunov, V. K. Polymorphism of Oxytungstates Tr₂WO₆. Mechanisms of Structural Changes in Y₂WO₆. *Crystallogr. Rep.* **1989**, *34*, 531–536.
- (10) Efremov, V. A.; Tyulin, A. V.; Trunov, V. K.; Kudin, O. V.; Yanovskii, V. K.; Voronkova, V. I. The Crystal Structure of Monoclinic Y₂WO₆ and Yb₂WO₆. *Kristallografiya* **1984**, *29*, 904–909.
- (11) Apostolov, Z. D.; Sarin, P.; Hughes, R. W.; Kriven, W. M. Thermal Expansion of Ln₆WO₁₂ and Ln₂WO₆—An In Situ Synchrotron X-ray Diffraction Study. *J. Am. Ceram. Soc.* **2014**, *97*, 2496–2505.
- (12) Rode, E. Ya.; Balagina, G. M.; Ivanova, M. M.; Karpov, V. N. System WO₃–La₂O₃ fig. 06484. *Zh. Neorg. Khim.* **1968**, *13*, 1451–1456.
- (13) Yoshimura, M.; Rouanet, A. Data Base of Phase Equilibria Diagrams of the American Ceramic Society: N° 93–047. *Mater. Res. Bull.* **1976**, *11*, 151–158.
- (14) Chambrier, M.-H.; Kodjikian, S.; Ibberson, R. M.; Goutenoire, F. Ab-initio Structure Determination of β -La₂WO₆. *J. Solid State Chem.* **2009**, *182*, 209–214.
- (15) Allix, M.; Chambrier, M. H.; Veron, E.; Porcher, F.; Suchomel, M.; Goutenoire, F. Synthesis and Structure Determination of the High Temperature Form of La₂WO₆. *Cryst. Growth Des.* **2011**, *11* (6), 5105–5112.
- (16) Tyulin, A. V.; Efremov, V. A.; Trunov, V. K. Polymorphism of Oxytungstates TR₂WO₆. Structure of Tetragonal Nd_{1.2}Lu_{0.8}WO₆. *Kristallografiya* **1989**, *34*, 81–86.
- (17) Halasyamani, P. S.; Poeppelmeier, K. R. Noncentrosymmetric Oxides. *Chem. Mater.* **1998**, *10*, 2753–2769.
- (18) Venkatesan, T.; Green, S. M. Pulsed Laser Deposition: Thin Films in a Flash. *Ind. Phys., American Institute of Physics* **1996**, *2*, 3–22.
- (19) Lowndes, D. H.; Geoghegan, D. B.; Puretzky, A. A.; Norton, D. P.; Rouleau, C. M. Synthesis of Novel Thin-Film Materials by Pulsed Laser Deposition. *Science* **1996**, *273* (5277), 898–903.
- (20) Desfeux, R.; Hamet, J. F.; Mercey, B.; Simon, C.; Hervieu, M.; Raveau, B. Thin Film Deposition of a New Cubic Perovskite, La_{4+x}Ba_{1-x}Cu₅O_{12+δ} used for the Realization of Multilayers with YBCO. *Phys. C (Amsterdam, Neth.)* **1994**, *221*, 205–214.
- (21) Balestrino, G.; Desfeux, R.; Martellucci, S.; Paoletti, A.; Petrocelli, G.; Tebano, A.; Mercey, B.; Hervieu, M. Growth of CaCuO₂ and Sr_xCa_{1-x}CuO₂ Epitaxial Films on NdGaO₃ Substrates by Pulsed Laser Deposition. *J. Mater. Chem.* **1995**, *5* (11), 1879–1883.
- (22) Shao, Z.; Saitzek, S.; Ferri, A.; Rguiti, M.; Dupont, L.; Roussel, P.; Desfeux, R. Evidence of Ferroelectricity in Metastable Sm₂Ti₂O₇ Thin Film. *J. Mater. Chem.* **2012**, *22* (19), 9806–9812.
- (23) Kalinin, S. V.; Rodriguez, B. J.; Borisevich, A. Y.; Baddorf, A. P.; Balke, N.; Jung Chang, H.; Chen, L.-Q.; Choudhury, S.; Jesse, S.; Maksymovych, P.; Nikiforov, M. P.; Pennycook, S. J. Defect-Mediated Polarization Switching in Ferroelectrics and Related Materials: From

Mesoscopic Mechanisms to Atomistic Control. *Adv. Mater.* **2010**, *22*, 314–322.

(24) Svensson, K.; Jompol, Y.; Olin, H.; Olsson, E. Compact Design of a Transmission Electron Microscope Scanning Tunneling Microscope Holder with Three-Dimensional Coarse Motion. *Rev. Sci. Instrum.* **2003**, *74*, 4945–4947.

(25) Detalle, M.; Rémens, D. Chemical and Physical Characterization of LaNiO₃ Thin Films Deposited by Sputtering for Top and Bottom Electrodes in Ferroelectric Structure. *J. Cryst. Growth* **2008**, *310*, 3596–3603.

(26) Gruverman, A.; Auciello, O.; Tokumoto, H. Imaging and Control of Domain Structures in Ferroelectric Thin Films via Scanning Force Microscopy. *Annu. Rev. Mater. Sci.* **1998**, *28*, 101–123.

(27) Desfeux, R.; Ferri, A.; Legrand, C.; Maës, L.; Costa, A. D.; Poullain, G.; Bouregba, R.; Soyer, C.; Remiens, D. Nanoscale Investigations of Switching Properties and Piezoelectric Activity in Ferroelectric Thin Films Using Piezoresponse Force Microscopy. *Int. J. Nanotechnol.* **2008**, *5*, 827–837.

(28) Horiba Scientific Avenue de la Vauve - Passage Jobin Yvon CS 45002 - 91120 Palaiseau – France.

(29) CaRIne Crystallography, version 3.1.

(30) Rodriguez, B. J.; Callahan, C.; Kalinin, S. V.; Proksch, R. Dual-Frequency Resonance-Tracking Atomic Force Microscopy. *Nanotechnology* **2007**, *18*, 475–504.

(31) Harnagea, C.; Pignolet, A.; Alexe, M.; Hesse, D.; Gösele, U. Quantitative Ferroelectric Characterization of Single Submicron Grains in Bi-Layered Perovskite Thin Films. *Appl. Phys. A: Mater. Sci. Process.* **2000**, *70*, 261–267.

(32) Martin, D.; Müller, J.; Schenk, T.; Arruda, T. M.; Kumar, A.; Strelcov, E.; Yurchuk, E.; Müller, S.; Pohl, D.; Schröder, U.; Kalinin, S. V.; Mikolajick, T. Ferroelectricity in Si-Doped HfO₂ Revealed: A Binary Lead-Free Ferroelectric. *Adv. Mater.* **2014**, *26*, 8198–8202.

(33) Gautier, B.; Duclère, J.-R.; Guilloux-Viry, M. Nanoscale Study of the Ferroelectric Properties of SrBi₂Nb₂O₉ Thin Films Grown by Pulsed Laser Deposition on Epitaxial Pt Electrodes Using Atomic Force Microscope. *Appl. Surf. Sci.* **2003**, *217*, 108–117.

(34) Gruverman, A.; Khoklin, A.; Kingon, A.; Tokumoto, H. Asymmetric Nanoscale Switching in Ferroelectric Thin Films by Scanning Force Microscopy. *Appl. Phys. Lett.* **2001**, *78*, 2751–2753.

(35) Ferri, A.; Saitzek, S.; Da Costa, A.; Desfeux, R.; Leclerc, G.; Bouregba, R.; Poullain, G. Thickness Dependence of the Nanoscale Piezoelectric Properties Measured by Piezoresponse Force Microscopy on (111)-Oriented PLZT 10/40/60 Thin Films. *Surf. Sci.* **2008**, *602*, 1987–1992.

(36) Hong, J.; Song, H. W.; Hong, S.; Shin, H.; No, K. Fabrication and Investigation of Ultrathin and Smooth Pb(Zr,Ti)O₃ Films for Miniaturization of Microelectronic Devices. *J. Appl. Phys.* **2002**, *92*, 7434–7441.

(37) Gruverman, A.; Rodriguez, B. J.; Nemanich, R. J.; Kingon, A. I. Nanoscale Observation of Photoinduced Domain Pinning and Investigation of Imprint Behavior in Ferroelectric Thin Films. *J. Appl. Phys.* **2002**, *92*, 2734–2739.

(38) Saitzek, S.; Shao, Z.; Bayart, A.; Ferri, A.; Huvé, M.; Roussel, P.; Desfeux, R. Ferroelectricity in La₂Zr₂O₇ Thin Films with a Frustrated Pyrochlore-Type Structure. *J. Mater. Chem. C* **2014**, *2*, 4037–4043.

(39) Yan, Y.; Wang, L.; Xue, J.; Chang, H. C. Ion Current Rectification Inversion in Conic Nanopores: Nonequilibrium Ion Transport Biased by Ion Selectivity and Spatial Symmetry. *J. Chem. Phys.* **2013**, *138*, 044706.

(40) Doi, K.; Tsutsui, M.; Ohshiro, T.; Chien, C.; Zwolak, M.; Taniguchi, M.; Kawai, T.; Kawano, S.; Di Ventra, M. Nonequilibrium Ionic Response of Biased Mechanically Controllable Break Junction (MCBJ) Electrodes. *J. Phys. Chem. C* **2014**, *118*, 3758–3765.

(41) Kohlstedt, H.; Pertsev, N. A.; Rodríguez Contreras, J.; Waser, R. Theoretical Current-Voltage Characteristics Of Ferroelectric Tunnel Junctions. *Phys. Rev. B: Condens. Matter Mater. Phys.* **2005**, *72*, 125341.